The astrochemical factory: A solid base for interstellar reactions

Ligterink, N.F.W.

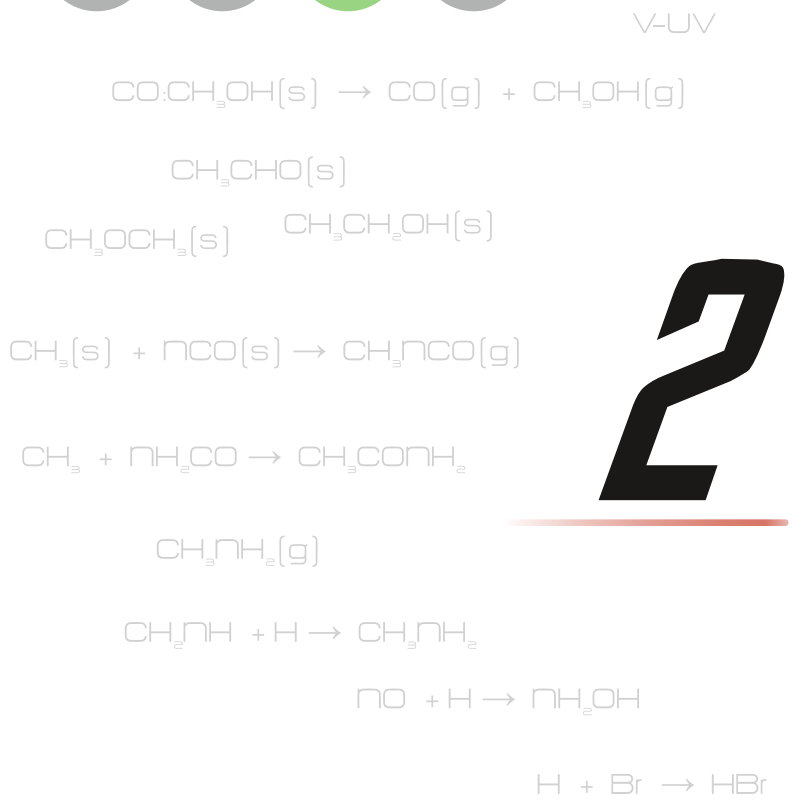

2

CryoPAD2 experimental set-up

N.F.W. Ligterink, M. Witlox & H. Linnartz

2.1. Introduction

The majority of the measurements in this thesis are carried out on the Cryogenic Photoproduct Analysis Device 2 (CryoPAD2, Fig. 2.1), a newly constructed and upgraded version of the original CryoPAD. This machine has as purpose to study Vacuum-UV (VUV, 115-180 nm, 6.9-10.8 eV) induced chemical and physical processes on interstellar dust grain analogues. The original CryoPAD has shown its merits over the past decade in a number of publications (Öberg et al. 2007, 2009a,c,b). The goal of CryoPAD2 is to build on these successes and add new capabilities to the machine, such as full spectral and flux calibration of the VUV source, addition of a high sensitivity mass spectrometer that can detect low abundance complex molecules, and improved, oil-free Ultra-High Vacuum (UHV) conditions.

In the following sections the technical details and capabilities of CryoPAD2 will be discussed. The calibration methods for the mass and IR spectrometers, and for the VUV photon flux are shown as well. Finally, the functioning of CryoPAD2 is demonstrated by a trial experiment.

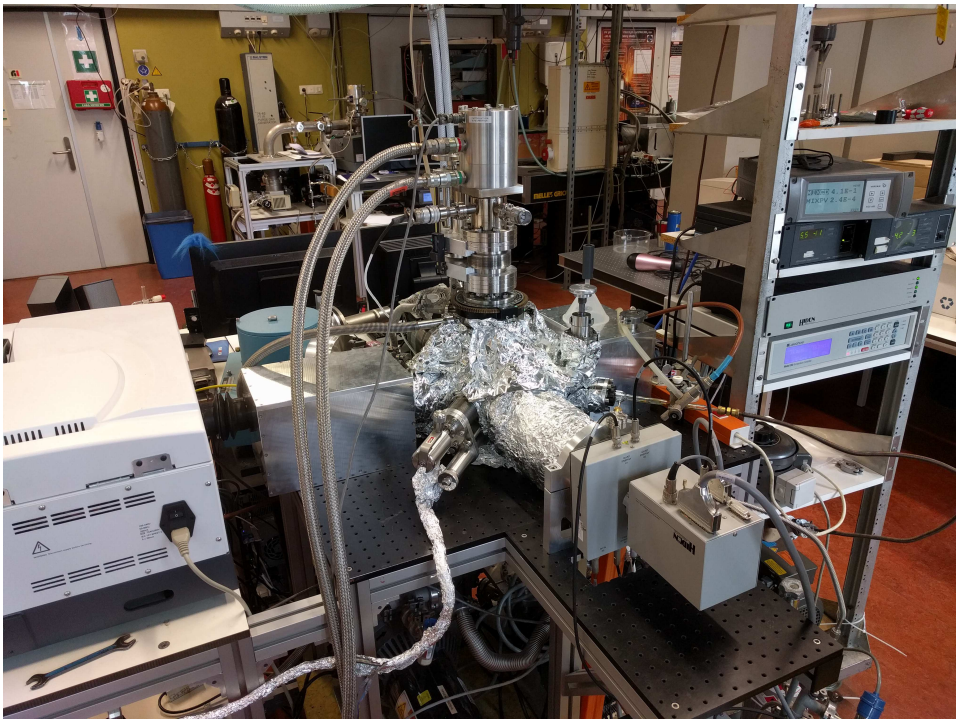

Figure 2.1: A picture of the CryoPAD2 set-up showing the UHV chamber at the center, on top the cryostate, in front the QMS and to the left the FTIR Spectrometer.

2.2. Description of CryoPAD2

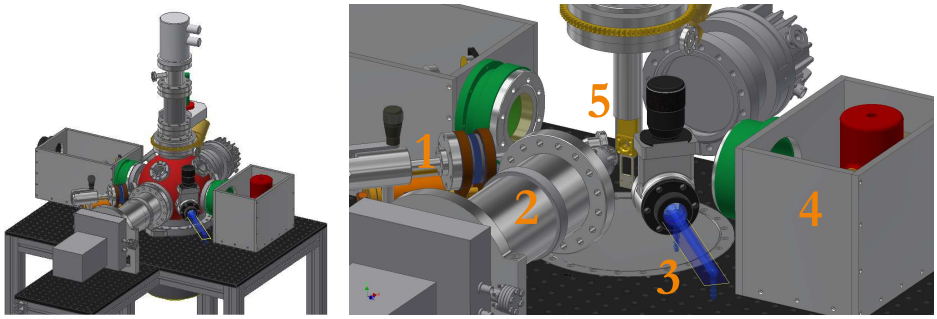

Figure 2.2: Mechanical drawing of the CryoPAD2 set up. 1) Deposition line, 2) QMS, 3) V-UV lamp, 4) IR detector in purge box, 5) Cryogenically cooled gold coated reflection surface.

CryoPAD2 consists of a main UHV chamber, typically $\sim 7 \times 10^{-11}$ mbar, to which all instruments are attached (see Fig. 2.2). Directly attached at the bottom of the chamber is an Agilent V1001 turbomolecular pump (900 L/s), which is backed by an oil free TS-300 dry-scroll pump (300 L/minute), also manufactured by Agilent. Horizontally attached to the chamber is a second Agilent TwisTorr 304 FS turbo pump, backed by the same scroll pump. The vacuum is monitored by a hot ion gauge, which is read out by a Granville-Phillips 350 ionization gauge controller and placed under a 45° angle with respect to the center line of the set-up. Three fused-silica view ports are located on other ports in the same plane.

At the top of the chamber an Advanced Research Systems (ARS) DE-202 cryostat is mounted via a translational and rotational UHV feed through. The feed through ensures that the cryostat can be rotated over 360° and vertically moved to allow the use of different instruments. Differential pumping of the rotational feed through occurs in two stages. The first stage is pumped by the TS-300 scroll pump and the second stage by a Varian V-301 turbomolecular pump, backed by an Agilent SH-110 dry-scroll pump. Attached to the tip of the cryostat, surrounded by a heat-shield, is a gold coated reflection substrate. This surface makes it possible to perform Reflection Absorption InfraRed Spectroscopy (RAIRS), which will be discussed shortly. Two thermocouples (Chromel-AuFe 0.07%) and a heating wire are attached to the substrate. The two thermocouples are located at the top and bottom of the reflection surface, while the heating wire is located a few centimetres above the top thermocouple. Read-out of the thermocouples and control of the heating wire is done by a Lakeshore Model 350 Cryogenic Temperature Controller. The lowest attainable temperature is around 12 K. Relative temperature read-out error of the thermocouples is $\pm$ 1 K and the absolute error is $\pm$ 2 K. The heating wire can heat the sample up to 300 K and higher.

Finally, at the bottom of the substrate a VUV grade AXUV-100 photodiode is mounted by thermally isolating PolyEther Ether Ketone, or PEEK, material, for photon flux measurements. The photodiode is calibrated by the

Physikalisch-Technische Bundesanstalt (PTB) for the range of 115 to 250 nm. Read out occurs through a Keithley 485 autorange picoammeter. Section 2.3.4 will go into further detail of the VUV photon flux determination.

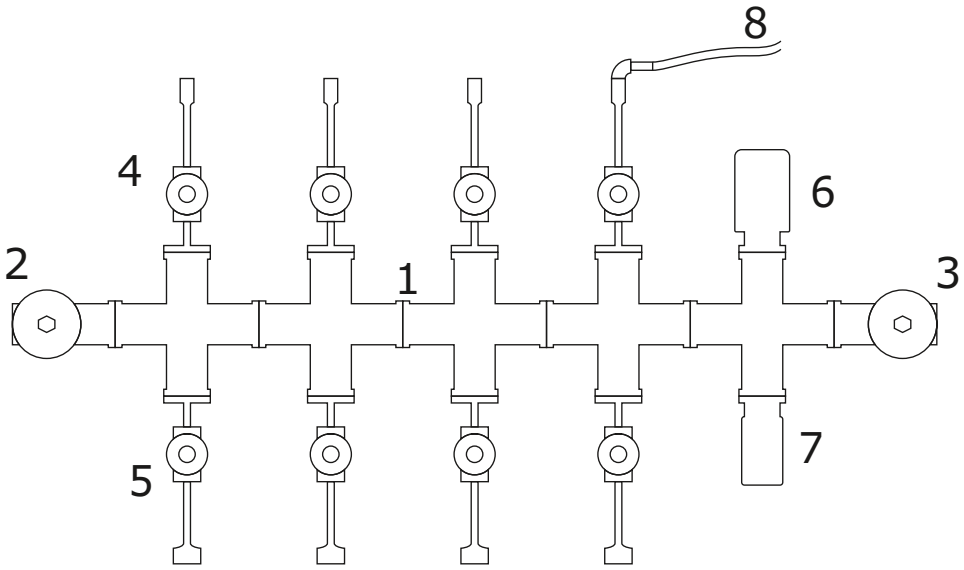

Figure 2.3: Schematic representation of the CryoPAD2 gas mixing line. The elements are: 1) Backbone consisting of CF38 cross pieces, 2) valve to prepump, 3) valve to turbo pump, 4) swagelok valve to three gas bottle connections, 5) swagelok valve to four tube connections for liquids and bulbs, 6) CDG-500 gas independent gauge, 7) PVG-500 pirani gauge, 8) swagelok valve and tube connection to the setup.

A deposition line connected to a high-precision gas-mixing system is used to grow ice layers on the cooled substrate. Pure and mixed gases are prepared in the gas-mixing system, see Fig. 2.3. The backbone of this system is a number of ConFlat cross-pieces (1). At both ends of the system valves are placed connecting to either a SH-110 dry-scroll pump for prepumping or a Varian V-301 turbomolecular pump, backed by a SH-110 scroll pump for High Vacuum (HV) pumping (2,3). Two connections house an Agilent PVG-502 pirani gauge (7), for monitoring the pressure, and a CDG-500 gas-independent diaphragm gauge (6) to create accurate gas mixtures. The remaining connections are used to attach gases (4) and liquids (5). Stainless steel Swagelok SS-4H-TH3 valves are in place here to regulate the gas-flow. gases are connected via a 6 mm Swagelok connection, while tubes with liquids are attached with a Cajon connection. From the gas-mixing system a tube (8) connects to an all-metal high precision leak valve, which extends into a deposition tube in the vacuum chamber. The leak valve is placed on a translation stage in order to move the deposition tube as close as possible to the substrate surface. At the end of the deposition tube a Micro Capillary Plate (MCP) is a placed to create a linear flow of gases and uniform deposition. In general deposition of gases is done from a distance of 5 mm and under an angle of 45° with respect to the surface.

Samples that are deposited can be treated with VUV radiation coming from

a Microwave Discharge Hydrogen-flow Lamp (MDHL). The MDHL will be extensively discussed in Chapter 3, but a short description is given here. This lamp is operated by flowing H_2 from the gas bottle through the glas lamp into an oil pump. On the lamp a microwave cavity is placed, which excites the hydrogen flow into a plasma. From this plasma excited H atoms and H_2 molecules release VUV light around 121 nm (Lyman-α) and between 140 to 170 nm (molecular hydrogen emission). Via a Magnesium Fluoride (MgF_2) window, that also acts as a vacuum seal, the VUV light enters into the vacuum chamber. This windows transmits light from visible wavelengths and down to 115 nm. Between the window and chamber a shutter is placed that acts as an "on/off" button for the MDHL.

Opposite from the MDHL a McPherson Model 234 0.2 meter VUV Monochromater is located to monitor the VUV spectrum of the lamp. The monochromater is connected via a tube and a MgF_2 window onto the vacuum chamber. This system is being pumped by a Leybold Turbovac 50 turbomolecular pump, which is backed by a SH-110 scroll pump. The monochromater covers a range of 30 to 550 nm. It makes use of a 1200 gr/mm grating and two adjustable slits, to obtain a spectral resolution of 0.1 nm at 313.1 nm center wavelength. At the end VUV light is collected by a Model 658 photomultiplier detector. Control and read out occurs with a Model 789A-4 Scan Controller and a Keithley 6485 picoammeter, which are connected to a LabView program. A typical VUV spectrum is shown in Fig. 2.4.

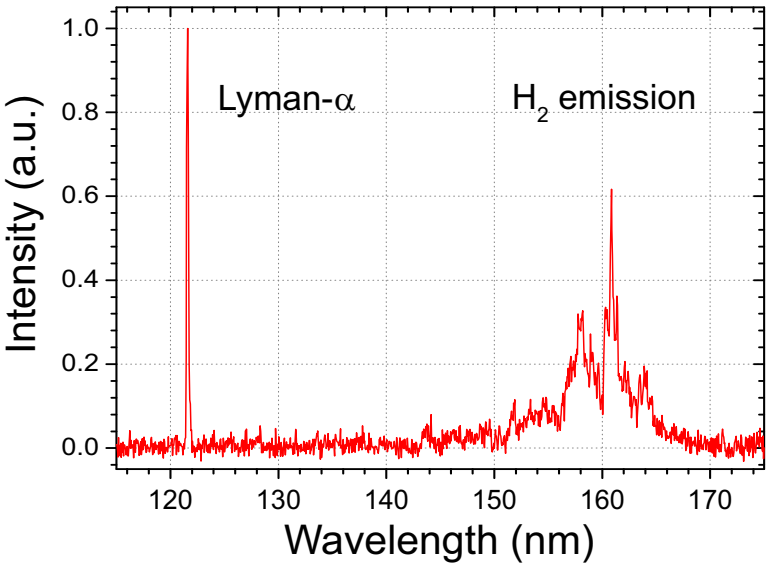

Figure 2.4: Typical spectrum of the MDHL measured with the McPherson Model 234 Monochromater. H-atom Lyman-α emssion is seen around 121.6 nm, while molecular hydrogen emission lines and continuum are seen between 140–170 nm.

Two detections techniques are used in this set-up. At the front side a Hiden HAL/3F RC 1000 PIC Quadrupole Mass Spectrometer (QMS) is located. It is capable of measuring gas-phase particles with masses between 1 and 300 amu

at high sensitivity. Gas-phase species are detected from 1) the background atmosphere of the chamber, 2) deposition of gases, 3) photodesorption of ice samples, and 4) Temperature Programmed Desorption (TPD) of the ice on the substrate. The latter two options are most important trace the physical and chemical changes in the ice. The electron source of the QMS is located roughly 6 centimeter from the reflection surface at the center of the chamber. As default, the electron source emits electrons at 70 V and a flux of 20 μA, but both settings are tunable. Altering the electron voltage can change the fragmentation pattern of gas-phase molecules entering the QMS, while the current can be increased to enhance the sensitivity to gas particles. Calibrations of the QMS are covered in Sections 2.3.1 and 2.3.2.

The second instrument is an Agilent 660 FTIRS system, set up in RAIRS via the reflection surface on the substrate. With the RAIRS set-up chemical and physical changes are traced in-situ in the ice. Two ZnSe windows are used to couple the light from the FTIR spectrometer into the set-up and out again toward a liquid nitrogen cooled Mercury Cadmium Telluride (MCT) detector. A number of gold-coated mirrors and off-axis parabolic mirrors guide the IR light from the FTIR to set-up and focus it on the substrate and MCT. The entire beam path of the RAIRS set-up outside the main chamber, including the FTIR itself, is purged with dry air to remove gas-phase IR features of water and carbon dioxide. With the FTIR a range of 500 to 4000 cm^{-1} or 2.5 to 20 μm can be covered. A spectral resolution as high as 0.1 cm^{-1} can be attained, although in practice 1 to 2 cm^{-1} resolution is used.

2.3. Calibrations

2.3.1. QMS work function

Each mass spectrometer has its own specific work function, or sensitivity per mass. Over large mass ranges the work function can vary substantially. This in turn can substantially alter mass fragmentation patterns and therefore needs to be adjusted for.

Mixtures of noble gases are used to measure their sensitivity and extrapolate these data points to cover the full mass range. A mixture of He:Ar:Kr:Xe at 88:4:4:4 ratio is used to measure at masses of 4, 40, 84 and 131 amu. Noble gases do not have fragmentation pattern, so this does not have to be corrected for. However, electron absorption cross sections are atom specific and do need to be taken into account. These values are taken from literature at 70 V as σ_{He} = 2.96 , σ_{Ar} = 25.2, σ_{Kr} = 34.5 and σ_{Xe} = 46.7 Å^2. When the gas mixture is leaked into the set-up and measured by the QMS, the resulting corrected signal $S_{\mathrm{corrected}}$ is obtained by:

$$S_{\mathrm{corrected}} = S_{\mathrm{QMS}} \times \frac{C_{\mathrm{mol}}}{\sigma_{\mathrm{mol}}}, \tag{2.1}$$

where S_{QMS} is the original QMS input, C_{mol} is a correction for the concentration (4 for Helium, 88 for the other three noble gases) and σ_{mol} is the electron absorption cross section of each atom. From the corrected signal the normalized ratios between the four atoms can be found and exponentially fitted,

see Fig. 2.5. This fit is used to correct mass traces when accurate mass ratios are needed.

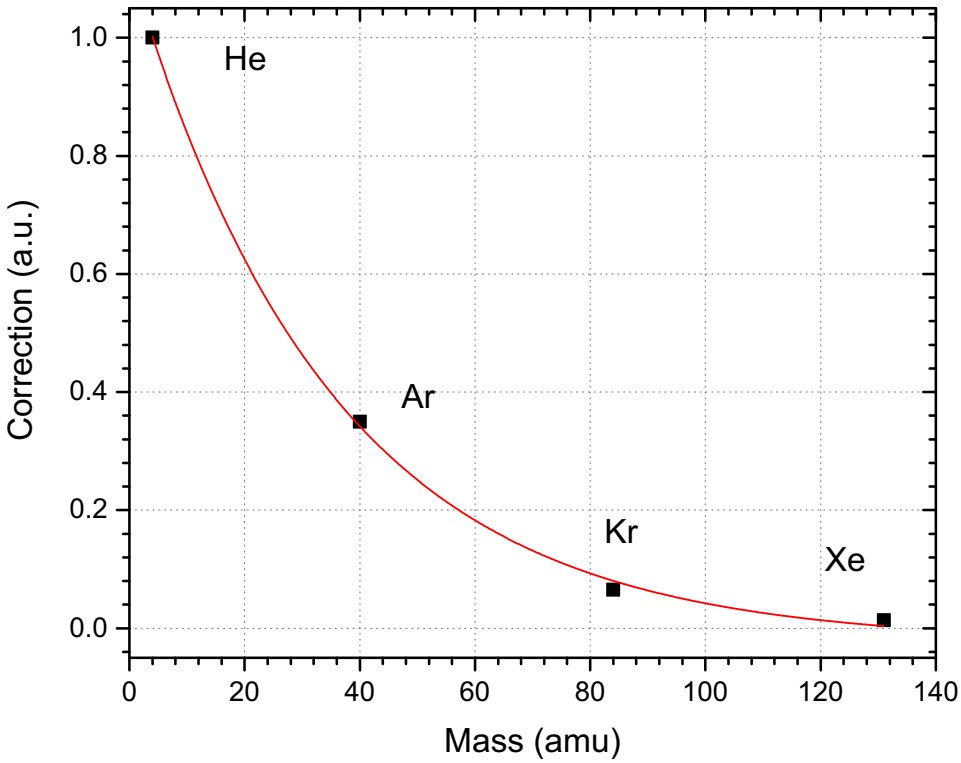

Figure 2.5: Workfunction of the Hiden QMS. Black squares indicate the normalized data points of the noble gases. An exponential curve is fitted through these points (red).

2.3.2. QMS filament output correction

The QMS system on CryoPAD2 has the ability to tune the electron output of the filament in its ionisation source. An increase of the electron current means that more gas-phase molecules can get ionised, thus effectively making the QMS more sensitive to a certain mass or masses. The opposite is possible as well, to decrease the current and become less sensitive to a certain mass. This is particularly useful to prevent the Secondary Electron Multiplier (SEM) detector from overranging, which occurs at measuring 1×10^7 counts s^{-1} (hits of fragments).

The effects of tuning the electron energy are investigated in order to determine 1) how the sensitivity changes with electron current, and 2) if fragmentation patterns change. $^{13}CH_3OH$ is leaked into the chamber while measuring its main masses at 30, 32 and 33 amu in sequence at filament currents of 5, 10, 20, 30, 40 and 50 μA. Data are used when the leak rate into the chamber has stabilised and a variety of leak rates are used in order to see if pressure effects play a role. All the masses are normalised to the standard electron current setting of 20 μA. Figure 2.6 shows the resulting sensitivity curve, which is slightly

exponential. Between each current setting the variation in the masses is minimal, so no change in fragmentation pattern is seen. Different leak rates showed negligible differences in sensitivity. Between measurements at 5 and 50 μA the sensitivity increases by a factor of 14.

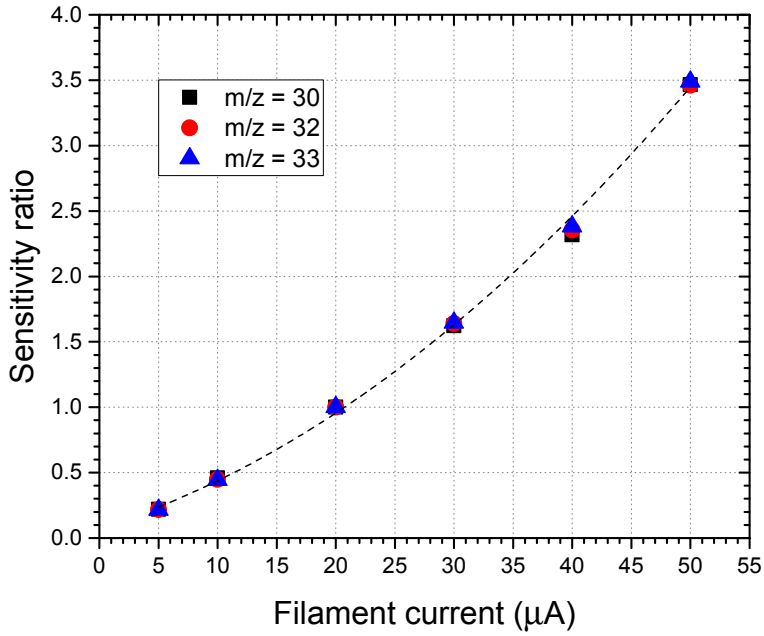

Figure 2.6: Sensitivity of the Hiden QMS at various filament currents, normalised to the value at 20 μA. The main fragments of $^{13}CH_3OH$ at m/z = 30, 32 and 33 are plotted versus filament current.

2.3.3. Column density and RAIRS correction

Column densities of parent species and products are in-situ determined by IR spectroscopy with the following equation:

$$N_{\text{species}} = 2.303 \frac{\int_{\text{band}} \tau d\nu}{A_{\text{band}}}, \tag{2.2}$$

where $N_{species}$ is the column density of the investigated species in molecules cm^{-2}, $\int_{band} \tau d\nu$ the integrated absorbance of the band in cm^{-1} and A_{band} the band strength in cm molecule^{-1}. IR band strengths listed in literature are usually determined in transmission. However, RAIRS set-ups make use of a reflection through the ice sample, which results in a longer path length and thus higher band strength values. Effectively this means that measuring the exact same amount of material in a transmission and RAIRS set-up results in a *larger* integrated absorbance peak in the RAIRS set-up. How much larger depends on

the geometry and technical details of the RAIRS set-up and is therefore set-up specific.

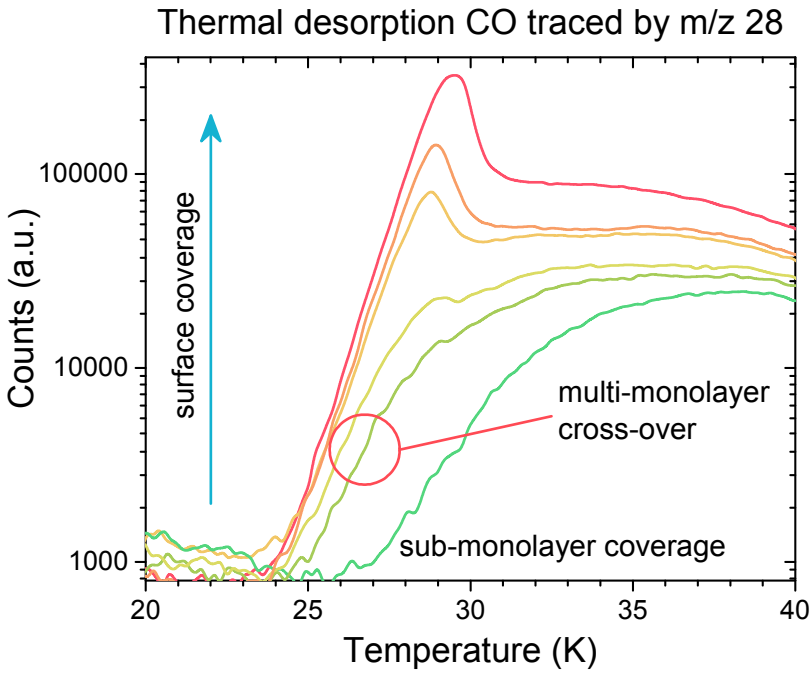

Figure 2.7: Desorption traces of CO for various surface coverages. The desorption temperature is seen to shift to higher values at lower coverage.

In CryoPAD2 the band strength of CO is determined by thermal desorption of thin CO films. Thick layers of a molecule are dominated by molecule-molecule binding energies, which are weaker than molecule-substrate bonds. Therefore a thin film, in the order of ∼1 ML thick, is more tightly bound to the substrate and exhibits a clear shift in desorption temperature compared to bulk ice. This effect is used to find the monolayer regime for CO, see Fig. 2.7. The desorption traces for a number of depositions are shown. The high coverage experiments start desorbing around 24 K, but at lower coverage the curve is seen shifting to 25 K. This is taken as the monolayer regime. At even lower, submonolayer, coverage the curve is seen to shift even further to 26 K.

The IR data of the monolayer curve are used to find its integrated absorbance band as 0.01497. By making the assumption that the monolayer is covered by 1×10^{15} molecules cm^{-2}, Eq. 2.2 can be used to find the band strength as $A_{\mathrm{RAIRS,CO}} = 3.4^{+0.5}_{-0.5}\times10^{-17}$ cm molecule^{-1}. Literature transmission values put the band strength at 1.12×10^{-17} cm molecule^{-1} (Bouilloud et al. 2015). Based on the set-up specific and literature transmission band strengths of CO and under the assumption that band strengths in the set-up scale all with the same factor, a

modified equation for the column density can be made:

$$N_{\text{species}} = 2.303 \frac{1.1}{3.4} \frac{\int_{\text{band}} \tau d\nu}{A_{\text{band}}}, \tag{2.3}$$

which now includes a correction factor of $\frac{1.1}{3.4}$. It is important to realise that this correction value can change by changes made in the geometry of the RAIRS set-up. Therefore the value should be remeasured each time such changes have been made.

2.3.4. VUV photon flux

Measuring the VUV photon flux starts by measuring the VUV photocurrent between 115 and 180 nm with the SXUV-100 photodiode. Since this photodiode is not only sensitive to high energy radiation, but also emission upto and beyond 1000 nm, it picks up visible emission from the MDHL. Therefore the VUV photon current I_{VUV} is determined by measuring the total photo current generated by the regular MDHL (I_{total}) and subtracting the visible part, here loosely defined as any wavelength $\geq$230 nm. The visible part is measured by using a MDHL which is closed-off with a fused-silica window (I_{vis}). This window does not transmit radiation below 230 nm, but has a transmittance of 0.9 ± 0.03 of the visible light beyond 230 nm. Both open and closed-off lamps are operated under the same conditions, e.g. flow pressure, input power. This leads to the following equation to measure the VUV photocurrent:

$$I_{\text{VUV}} = I_{\text{total}} - \frac{I_{\text{vis}}}{0.9}, \tag{2.4}$$

The VUV photocurrent consists of contributions at different wavelengths in the VUV spectrum. Therefore the current needs to be assigned in a percentage wise fashion to each wavelength in the spectrum. To give an example, if the Lyman-α peak at 121 nm contributes 25% of the total spectrum between 115 and 230 nm, then $0.25 \times I_{\text{VUV}}$ will be assigned to it. The VUV spectrum that is used depends on the settings of the MDHL (see Chapter 3 for MDHL settings and VUV spectra). From the following equation the wavelength dependent flux, $\Phi(\lambda)$, is determined:

$$\Phi(\lambda) = \frac{I(\lambda)}{e\epsilon(\lambda)}, \tag{2.5}$$

where e is the electron charge and $\epsilon(\lambda)$ the wavelength dependent quantum efficiency. By integrating over the range between 115 and 230 nm the total VUV photon flux can be determined. As an example, for an VUV photocurrent of I_{VUV} = 1.05 μA a VUV photon flux of $1.1 \pm 0.1 \times 10^{14}$ photons cm^{-2} s^{-1} is derived. Besides being dependent on the MDHL settings, this flux number can change over time due to differences in orientation of the sample, the use of collimator tubes or simply contamination of the lamp. Therefore it needs to be measured at regular intervals.

2.4. An experimental example

To demonstrate the capabilities of CryoPAD2, results of an VUV processing experiment of a thin, pure isocyanic acid (HNCO) film are presented. Examples are given on how to handle RAIRS spectroscopy and TPD mass spectrometry data. This section will conclude by showing what can be learned from these kind of experiments.

2.4.1. Introduction

HNCO is abundantly found in the gas-phase in the ISM (Bisschop et al. 2007b; Bergner et al. 2017). In its ionic form, OCN^- has been detected in interstellar ices (Boogert et al. 2015). Several observational studies have linked HNCO to the formation of more complex prebiotic species such as formamide (NH_2CHO López-Sepulcre et al. 2015; Coutens et al. 2016) and state that formation occurs in the ice phase. Laboratory experiments have shown that HNCO can undergo efficient acid-base reaction with NH_3 to form $OCN^-NH_4^+$ salts (van Broekhuizen et al. 2004). VUV irradiation of HNCO shows that OCN^- is one of the main products, but also more complex species like NH_2CHO and NH_2CONH_2 form (Raunier et al. 2004). These reactions have so far only been studied in a qualitative way.

2.4.2. Experimental

A pure sample of HNCO is prepared by thermally cracking cyuranic acid, a trimer of HNCO. With freeze-pump-thaw cycles impurities, mainly CO and CO_2, are removed from the gas. The gas is deposited on the substrate at 15 K, after which it is irradiated for 20 minutes in 1 minute intervals. After each interval an IR spectrum is taken between 700 and 4000 cm^{-1} at a resolution of 0.5 cm^{-1} in order to trace chemical changes in the sample. These spectra are baseline subtracted, for which an example is shown in Fig. 2.8. Column densities are determined according to Sect. 2.3.3 from the integrated band area. Expected molecular products and their band positions and strengths are listed in Table 2.1.

The VUV flux for this experiment is determined to be 2.86×10^{14} photons s^{-1} cm^{-2}, according to Sect. 2.3.4. In 20 minutes of irradiation this amounts to a fluence of 3.4×10^{17} photons cm^{-2}. The VUV spectrum is dominated by H_2 transitions around 150-160 nm and no Lyman-α is present, see Fig. 2.9. The absence of Lyman-α could be reflected in the chemistry, because strongly bonded molecules may not be broken.

The QMS is set to measure known and expected products of HNCO processing. In Table 2.2 expected products are listed together with their main fragment masses and desorption temperatures for pure ices. At the end of the irradiation time a TPD is set at a rate of 10 $Kmin^{-1}$. The QMS data are corrected for the work function according to Sec. 2.3.1.

2.4.3. Results

Figure 2.10 presents the IR spectrum of HNCO after deposition and after 20 minutes of VUV irradiation for the region between 2100 and 2400 cm^{-1}. Some

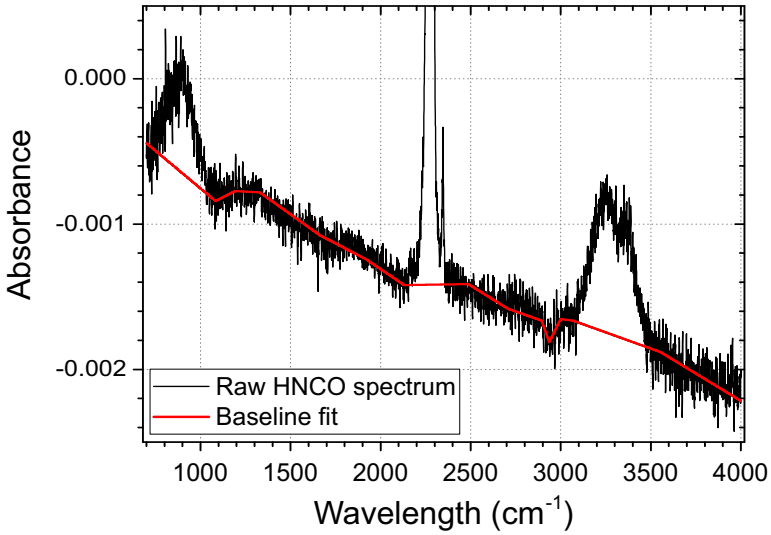

Figure 2.8: Baseline fit of the HNCO deposition

CO_2 contamination is visible in the deposition spectrum. No CO and OCN^- are visible. From the HNCO integrated peak area a column density of 2.6 $\times$ 10^{15} cm^{-2} is determined. After irradiation, the HNCO peak has decreased, while the formation of OCN^- and some additional CO_2 is seen. The OCN^- counter ion, NH_4^+, is not seen at 1470 cm^{-1} and neither is CO is at 2142 cm^{-1}. The latter may be blended in the OCN^- peak, however. Two other potential products, HNC and its isomer HCN, are not seen either. Around 1700 cm^{-1}, where H_2CO, NH_2CHO and NH_2CONH_2 have prominent CO stretching modes, no feature shows up over the course of irradiation, indicating that little or none of these species are formed. Based on an upper limit integrated absorbance area of 0.01, the upper limit column densities for HCN/HNC and NH_2CHO are determined to be $\leq 1.5\times10^{15}$ and $\leq 1.1\times10^{14}$ molecules cm^{-2} at the end of irradiation. Due to possible blending with OCN^-, a more conservative upper limit integrated absorbance of 0.02 is used for CO, resulting in an upper limit column density of $\leq 1.3\times10^{15}$ cm^{-2}.

The normalized TPD trace of m/z 27, 28, 45 and 60 are shown in Fig. 2.11 and correspond to masses of the molecules HCN/HNC, CO, NH_2CHO and NH_2CONH_2 that were not seen in the IR spectra. The position where the bulk of HNCO desorbs (m/z 43) at 115 K is indicated by a red dotted line. HCN is not seen desorbing around 140 K, but a significant signal is seen at 115 K. However, since m/z 27 is also present in the HNCO fragmentation pattern, HCN/HNC can at most partially contribute to this feature. In the m/z 28 signal a peak is seen around 40 K that can be attributed to CO desorption, although N_2 can not be ruled out either. Formamide is seen in the m/z 45 trace where it releases at 210 K. The other two peaks at this mass correspond with $^{13}CO_2$ and co-desorption of formamide. NH_2CONH_2 can not clearly be claimed in the m/z 60 trace. A low intensity feature does show up around 270 K, but is not strong enough to claim a detection.

Table 2.1: IR band positions and band strengths of HNCO and photolysis products

Molecule	Mode	Position cm^{-1}	Band strength $\times 10^{-17}$ cm molecule^{-1}
NH_4^+	bend.	1470[d]	-
NH_2CHO	CO str.	1708	6.54[e]
HNC	NC str.	2029	-
HCN	CN str.	2099	0.51[b]
CO	CO str.	2142	1.12[a]
OCN^-	OCN str.	2162	13[c]
HNCO	NCO str.	2282	7.8[c]
CO_2	CO str.	2342	7.6[a]

Notes. [a]Bouilloud et al. (2015), [b]Gerakines et al. (2004), assumed to be the same for HNC, [c]van Broekhuizen et al. (2004), [d]Raunier et al. (2004), [e]Brucato et al. (2006)

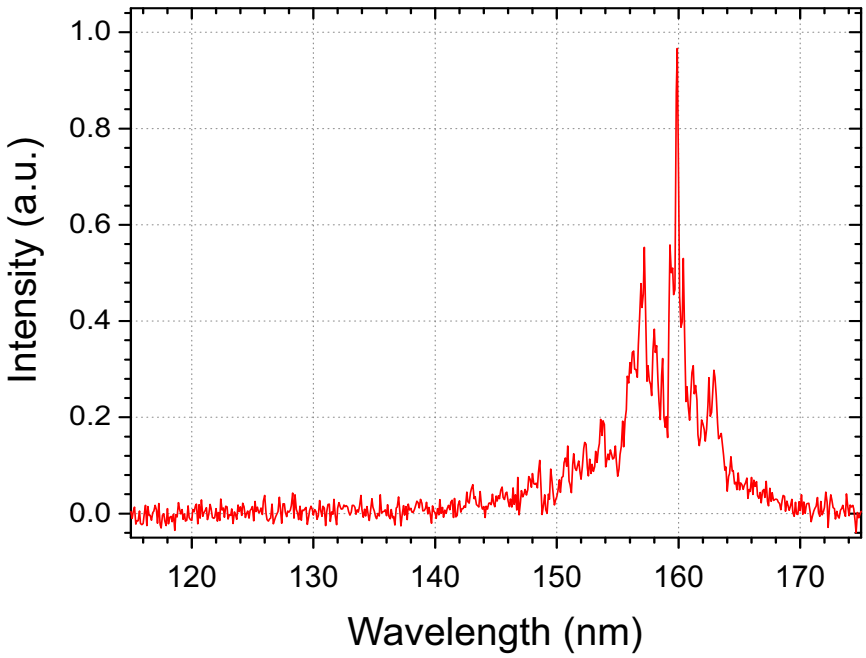

Figure 2.9: Spectrum of the VUV light used in the irradiation of HNCO.

Table 2.2: Molecular mass and desorption temperatures

Molecule	CO/N_2	HCN	CO_2	HNCO	NH_2CHO	NH_2CONH_2
m/z	28	27	44,28	43,42	45	60
T_{des} (K)	30[a]	140[b]	75[c]	115	210[d]	>240

Notes. [a]Öberg et al. (2005), [b]Theule et al. (2011),[c]Collings et al. (2004),[d]lab verification experiments.

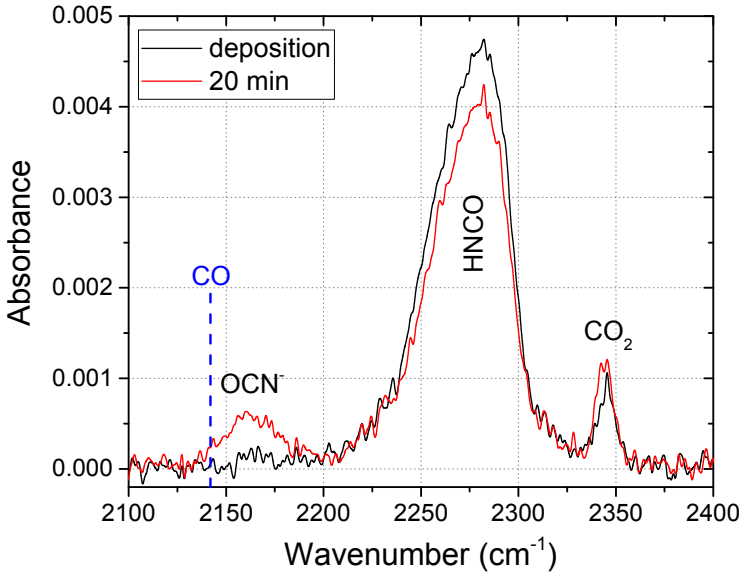

Figure 2.10: Spectra of HNCO after deposition and 20 min irradiation.

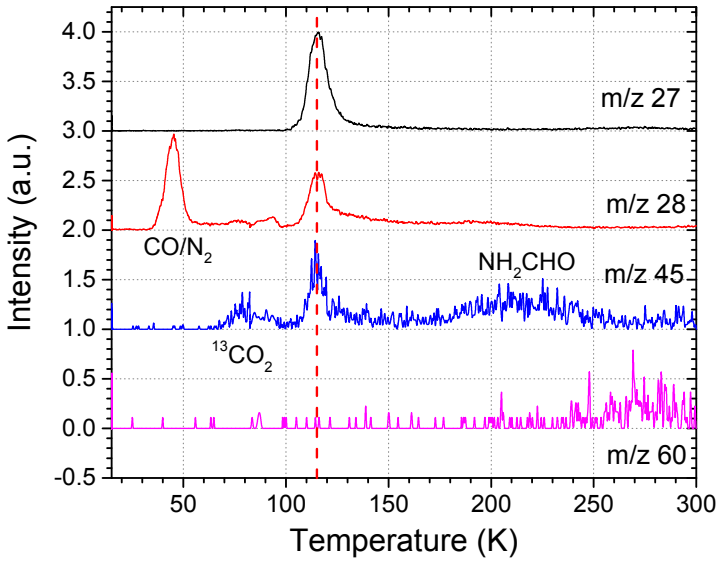

Figure 2.11: TPD traces of m/z 27, 28, 45 and 60. The dashed red line indicates the HNCO desorption peak.

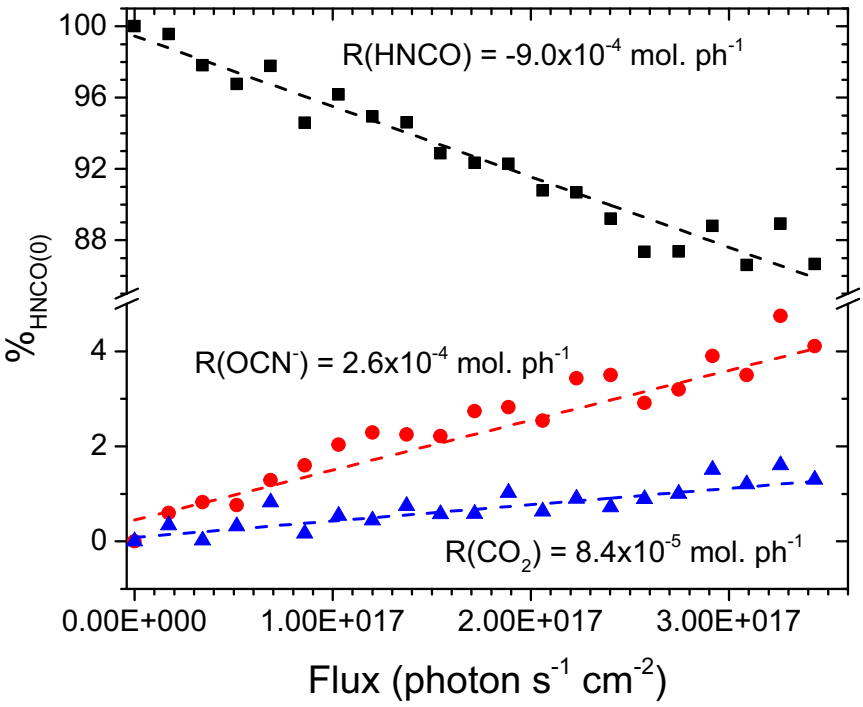

Figure 2.12: Photodestruction rate of HNCO and photoproduction rate of OCN^- and CO_2. The uncertainty of each data point amounts to ∼20%.

2.4.4. Discussion

Figure 2.12 plots the column densities of HNCO, OCN^- and CO_2 as a percentage of the starting amount of HNCO. A photodestruction rate is determined for HNCO, while photoformation rates are obtained for OCN^- and CO_2. They are -9.7×10^{-4}, 2.6×10^{-4} and 8.4×10^{-5} molecules photon^{-1}, respectively, with an estimated uncertainty of ∼20%. The (upper limit) formation rates of (non-)detected species are listed in Table 2.3.

Experimental results like these can help understand the reaction network of isocyanic acid. A number of possible HNCO reactions are listed in Table 2.4. The formation CO_2 (reaction [10]) can only be caused by the presence of oxygen atoms, as produced by reaction [3], although contributions of contaminants like water can not entirely be ruled out based on one experiment. OCN^- formation indicates that ammonia needs to be present to undergo the acid-base reaction, see reactions [8] and [9]. This in turn means that reaction [1] and/or [2] are occurring to produce N and N* that lead to NH_3. In this case contamination does not play a role since the only nitrogen-bearing contaminant is N_2, which can not be dissociated by VUV light of our lamp. Therefore the only source of nitrogen is HNCO. During processing of the ice much of the hydrogen reservoir gets locked up in ammonia and formamide. Both molecules need two additional hydrogen atoms to form from NH or HNCO, respectively. Assuming contaminations like water play a limited role, there must remain a large NCO reservoir, at least

Table 2.3: Column densities after 20 min irradiation and production/destruction rates

Molecule	N_{final} $\times 10^{15}$ mol. cm^{-2}	$R_{molecule}$ $\times 10^{-4}$ mol. ph^{-1}
HNCO	1.92	-9.0
CO	$\leq$1.3	$\leq$38
HCN	$\leq$1.5	$\leq$44
HNC		
CO_2	0.03	0.84
OCN^-	0.1	2.6
NH_2CHO	0.11	$\leq$3.2

Table 2.4: Overview of possible HNCO reactions

Nr.	Reaction	Products	Note
1	HNCO + VUV	H + NCO $\rightarrow$ N + CO	
2		HN + CO	
3		HNC + O	*Needed for* CO_2 *formation*
4	HNCO + VUV + H	$H_2NCO/HNCHO \rightarrow NH_2CHO$	*Net H loss channel*
8	HNCO + NH_3	$OCN^-NH_4^+$	
9	(H)N + H	NH_3	*Net H loss channel*
10	CO + O	CO_2	

Notes. Species that have been detected in the experiment are indicated in red.

1×10^{14} for ammonia (based on the OCN^- column density). This NCO reservoir must be locked up in double and triple bonded molecules, most likely N_2 and CO.

2.4.5. Conclusion

CryoPAD2 has been constructed and commissioned. This final section has shown a typical experiment as conducted on the set-up. From the data kinetics results, specific photodestruction and production rates can be inferred. With the QMS it is possible to detect low abundance products in the TPD. This shows the potential of this set-up to investigate reaction dynamics in interstellar ice analogues up to low abundance complex molecules.